Minerals Engineering 210 (2024) 108647

Contents lists available at ScienceDirect

Minerals Engineering

journal homepage: www.elsevier.com/locate/mineng

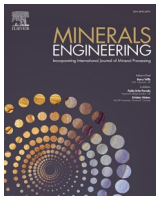

# Trace element impurities in anode copper from Olympic Dam, South Australia

Nigel J. Cook [a,*], Kathy Ehrig [a,b], Cristiana L. Ciobanu [a], Sarah E. Gilbert [c], Hassan Gezzaz [a]

[a] School of Chemical Engineering, The University of Adelaide, Adelaide S.A. 5005, Australia
[b] BHP Olympic Dam, 10 Franklin Street, Adelaide S.A. 5000, Australia
[c] Adelaide Microscopy, The University of Adelaide, Adelaide S.A. 5005, Australia

ARTICLE INFO

*Keywords:*
Anode copper
Impurities
Microanalysis
Laser ablation inductively coupled plasma mass spectroscopy
Olympic Dam

ABSTRACT

Anode copper is the intermediate product between copper smelting and electrorefining. Anodes are typically 98.5 to 99.8 % pure and require electrorefining to high-purity copper cathode that can be sold to customers. Impurity elements, including Ag, Au, As, Sb, Bi, Se, Te, Sn, Pb, Co, and Ni (alongside minor Fe, Al, and Si), are either dissolved within anode copper, or contained within micron-scale inclusions. To better understand the distribution of these impurities, a study of anode copper was undertaken on representative samples from the Olympic Dam anode plant, South Australia. Bulk assay for 61 elements of 269 sub-samples collected on a grid across a single anode, including the 'ears', shows homogeneity irrespective of location. The five most abundant impurity elements are As (mean 1279 ± 41 ppm), Se (218 ± 11 ppm), Sb (211 ± 8 ppm), Bi (202 ± 9 ppm), and Ni (195 ± 6 ppm). The assay data demonstrate that reliable, representative compositional data on the anode can be obtained from sampling and assay of only a limited part of the whole, including the 'ears'.

Trace element analysis of copper metal by laser ablation inductively coupled plasma mass spectrometry (LA-ICP-MS) allows quantification of dissolved minor components. Some metals, notably Ni, occur almost completely dissolved in copper. Other elements occur only partially in dissolved form, but the proportions measured in copper metal relative to bulk assay vary significantly from only ~ 9 % for Pb, 13 % for Bi and Te, 25 % for Se, 29 % for Sn, 34 % for Sb, 55 % for As, and 60–70 % for Au, Ag, and Co. These results are consistent with the observation of a diverse suite of 1–10 μm-sized, rounded impurity inclusions containing Pb, Bi, As, Sb, Te, Se etc. that are associated with cuprite, $Cu_2O$, and largely follow copper grain boundaries. The inclusions, each containing one or more crystalline (e.g., Cu-selenides, some Cu-Bi-arsenates, Sn-oxides and cuprite) and/or glassy phases (e.g., Cu-Pb-As-Sb-Bi-oxides), represents a trapped melt droplet, leading to the observed broad range of compositions.

## 1. Introduction

Characterization and deportment studies targeting minor components in millfeed and throughout flotation-smelting-electrorefinery circuits have attracted recent research interest for two reasons. Firstly, detailed information assists in the design of new pathways for removal of deleterious impurities efficiently, cost-effectively, and with lesser environmental impact. Secondly, operators are increasingly aware of the potential opportunity to recover valuable components (e.g., critical minerals) as by-products from existing operations. Such a proposition is particularly pertinent for large, long-term mine-to-metal operations, in which knowledge about the distribution the occurrence and distribution of both deleterious and potential by-product components can have decadal impact on optimization of operations and maximization of long-term revenue streams.

In copper processing-smelting refinery operations, noble (Au, Ag, platinum group elements) and other metals and metalloids, as well as the chalcogens selenium (Se) and tellurium (Te), report to flotation concentrates, and after smelting, accumulate in anode copper, the impure (~99.7 % Cu) intermediate product prior to electrorefining and production of high-purity (99.999 % Cu) copper metal (Schlesinger et al., 2022). The same group of elements finally report to anode refinery slimes during electrorefining (Hait et al., 2009). Noble metals and in some cases, other valuable elements such as Te, are recovered by

* Corresponding author.
*E-mail address:* nigel.cook@adelaide.edu.au (N.J. Cook).

https://doi.org/10.1016/j.mineng.2024.108647
Received 12 October 2023; Received in revised form 27 February 2024; Accepted 28 February 2024
Available online 9 March 2024

processing the anode slimes.

A substantial body of published data exists on the deportment of impurity elements in copper anodes from some of the world's largest smelter operations (e.g., Chen and Dutrizac, 1988, 1990b, 2005; see also review by Moats et al., 2012). Despite this, rapid advances in the sensitivity and spatial resolution of contemporary microanalysis and materials characterization techniques make it possible to determine the compositions of anode-bound impurity phases both accurately and reliably.

The Olympic Dam mining-processing-smelting-refinery operation in outback South Australia, exploits a giant (>10 billion tonne) ore deposit (Ehrig et al., 2012), and is currently producing copper cathodes, $U_3O_8$ concentrate, and gold and silver bullion. The deposit is also relatively enriched in a wide variety of other elements relative to crustal values, including Se, Te, arsenic (As), antimony (Sb), bismuth (Bi), cobalt (Co), nickel (Ni), tin (Sn), and rare earth elements. None of these elements are recovered at the present time.

This contribution is part of a larger study tracking the distribution of selected minor components from ore through concentration, leaching, smelting and electrorefining to final product. Here, we address the distribution of Ag, Au, As, Sb, Bi, Se, Te, Sn, Pb, Co, and Ni in representative samples of anode copper. Our observations and interpretations are based on a suite of assay data addressing composition at the scale of the entire anode, and *in-situ* laser ablation inductively coupled plasma mass spectroscopy (LA-ICP-MS) trace element analysis of copper metal at the scale of tens of microns. Our objective is to demonstrate compositional homogeneity across the anode and establish partitioning trends between metallic copper and inclusion-hosted impurities.

Cook et al. (2024) have addressed the appearance and composition of the same suite of elements in electrorefinery operations at Olympic Dam by analysis of raw anode slimes, decopperised slimes, and pH-neutralized slimes prior to cyanidation and precious metal recovery. Collectively, a sound understanding of phase speciation and association in copper anodes and refinery slimes can contribute to the development of innovative approaches to remove impurities and/or recover valuable elements that would otherwise be discarded. No prior information on the composition, appearance and contained impurity elements in copper anodes from Olympic Dam is available in the public domain.

## 2. Background

### 2.1. Impurities in copper anodes

Impure copper anodes are produced by pyrometallurgical methods and have purities that typically range from 97.7 to 99.7 % Cu (Moats et al., 2019), although purities can be significantly lower in some smelter operations (e.g., the example with 90.05 wt% Cu described by Campbell and Moats, 2019). Impurity concentrations (typically Ag, Au, As, Sb, Bi, Sn, Se, Te, Co, Fe, Ni, O, and Pb) depend on the source concentrate and prior processing and thus vary widely from operation to operation. Impurities in copper anodes have been the subject of prior study (e.g., Chen and Dutrizac, 1989, 1990a, 1990b, 1993, 2005), although relatively little quantitative data exists in the published literature. Each inclusion and the combination of incompatible impurities contained within it represents a trapped melt droplet. Inclusion phases are the final phases to solidify after anode casting and are therefore typically observed at grain boundaries in the copper (e.g., Chen and Dutrizac, 1990b; Wenzl et al., 2007a, 2007b, 2008). Minor amounts of oxygen in the molten copper facilitate formation of included cuprite, $Cu_2O$ (e.g., Chen and Dutrizac, 1990b).

Some metals, notably Ag and Au, but potentially also platinum group metals if present, are likely to occur almost exclusively within copper metal (Chen and Dutrizac, 1990b) with subordinate concentrations as discrete Ag- and/or Ag-Au-selenide inclusions or substituted within Cu-selenides. Most other impurities, including As, Sb, Bi and Pb, occur both in solid solution within copper and as inclusions. Nickel, if present at low to moderate concentrations, will also be largely in copper metal. Inclusions of NiO and chalcophyllite (kupferglimmer) only occur when Ni concentrations in anode copper exceed 2500–3000 ppm (Chen and Dutrizac, 1990a).

### 2.2. Mine-to-metal processing at Olympic Dam

The underground 10 Mt-per-year mining operation at Olympic Dam exploits a heterogeneous breccia-hosted sulphide ore (Ehrig et al., 2012). Processing circuits at Olympic Dam are described in BHP Billiton (2009). Ores are crushed and ground to a $D_{80}$ of 32 μm prior to froth flotation. Uranium is recovered via mildly aggressive oxidative, sulphuric acid leaching of Cu-sulphide depleted flotation tailings, followed by extraction from leach liquors via solvent extraction, ammonium diuranate precipitation, and calcination to produce uranium ore concentrate (UOC). Uranium is also recovered from sulphuric acid leaching (pH 1–2, ~65 °C) of flotation concentrates, a step also designed to remove fluorite prior to smelting.

Prior to smelting, leached copper concentrates are dewatered using thickeners and filters. Silica flux and dust from the waste-heat boiler and dust collectors are added. Olympic Dam smelter operations involve a single direct-to-blister smelting process that offers significant energy, $SO_2$ collection, and cost advantages over traditional two-stage processing (Schlesinger et al., 2022). Copper concentrates in slurry form are fed into the feed preparation thickener. The thickened concentrate is then pumped to batch filters to produce a filter cake, which is sent to steam coil driers. Dry concentrate is transported to storage silos at the top of the building ready for smelting.

Together with silica flux and recycled furnace dust, the concentrates are fed into the flash furnace burner under air enriched in oxygen leading to instantaneous combustion (residence time 1 s). The flash furnace (FF) operates at 1300 °C under an oxidizing atmosphere to liberate sulphur from Cu-sulphides and form sulphur-based molten blister. Iron oxide reacts with $SiO_2$ added as fluxing agent and other acidic and basic oxides in the concentrates to form slag. Blister copper (~99 % pure) and slag (comprising iron-oxides, silicates, glasses and residual copper) separate into two molten layers on the hearth of the furnace. Flash furnace slag is further processed by manual tapping to an electric slag reduction furnace (EF) that uses a coke reductant to recover remaining copper.

Blister copper from the FF and EF is tapped into one of two anode furnaces via a fully enclosed launder system heated by LPG-fired burners. In the anode furnace air, nitrogen and LPG are injected into the copper in a controlled sequence to remove sulphur and residual oxygen. After removal of sulphur and most of the oxygen, molten copper is cast onto a twin casting wheel to produce anodes (365 kg each). (Fig. 1). Further refining of anode copper (purity approximately 99.6 %) takes place in the on-site electrorefinery, where it is converted to A-grade cathode copper for market. The anode slimes that accumulate upon removal of the remaining insoluble impurities are treated and precious metals recovered.

During the smelting process, many of the elements focussed on in this contribution (Se, Te, As, Bi, Sb, Sn, Pb, Ag, and Au) are concentrated in blister copper. Others, including Co and Ni, occur in copper but also within various slag phases, including magnetite, fayalite, delafossite, and glasses (Gezzaz et al., 2023a, 2023b).

## 3. Analytical methodology

### 3.1. Sampling and bulk analysis

All results reported here were obtained from a copper anode produced in mid-2022. To assess compositional homogeneity across a 45.3 mm-thick, anode weighing 360 kg (Fig. 2A), and thus ensure that a < 100 g sub-sample is truly representative of the whole anode, a total of 249 samples were extracted (Fig. 2B), first by water jet cutting, and then

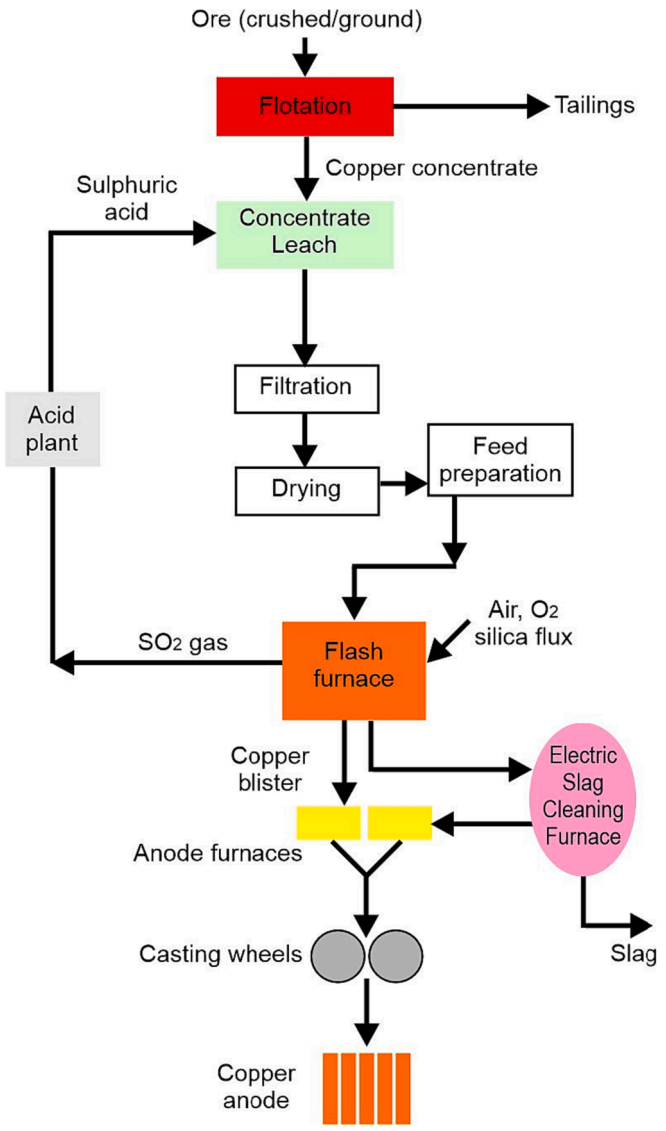


**Fig. 1.** Simplified diagram illustrating the sequence of operations at Olympic Dam from concentrator to anode copper.

by drilling out from strips cut from the anode (Fig. 2C), all shavings being collected. These samples were assayed for a suite of 61 elements at Genalysis-Intertek (Adelaide), involving five different analytical methods (see footnote to Table 1). The samples covered a grid pattern across the 907 x 947 mm-sized anode, the bottom, middle and top (relative to thickness), as well as the anode ears. Assay results confirmed homogeneity in all three dimensions across the anode, and that sampling of the ears is representative of the full anode.

Ten fragments from sample C6 (Fig. 2D) were selected and cut for mounting in epoxy. All subsequent petrographic and microanalytical work was performed on these sub-samples. This suite of sub-samples is representative of the anode tops (surface exposed to air) and bottoms (surface in contact with casting mould). The sample suite comprised representative examples in which the polished face was parallel to the anode top/bottom as well as perpendicular (Fig. 2D, E).

### 3.2. Electron probe microanalysis and LA-ICP-MS trace element analysis

Anode fragments were mounted in epoxy and imaged in backscatter electron (BSE) mode using an FEI Quanta 450 Field Emission Gun scanning electron microscope equipped with a silicon-drift energy-dispersive X-ray spectrometer.

Quantitative compositional data for cuprite and Cu-selenide inclusions was determined using a Cameca SX-Five electron probe microanalyzer (EPMA), equipped with five tuneable wavelength-dispersive spectrometers. Analysis was performed using operating conditions of 15 kV and 20nA, a beam diameter of 2 μm, and combination of natural and synthetic standards. X-ray lines were: S Kα, Ba Lα, Pb Mα, Sb Lα, Sn Lα, Bi Mα, Ag Lα, Te Lα, Cr Kα, Cu Kα, Au Lα, Al Kα, As Lα, Se Lα, Fe Kα, Ni Kα, and Co Kα. Typical minimum detection limits (in wt.%) were: $SO_3$ 0.03, BaO 0.05, PbO 0.07, $Sb_2O_3$ 0.04, $SnO_2$ 0.05, $Bi_2O_3$ 0.07, $Ag_2O$ 0.06, $TeO_2$ 0.05, $Cr_2O_3$ 0.04, $Cu_2O$ 0.06, $Au_2O_3$ 0.05, $Al_2O_3$ 0.03, $As_2O_3$ 0.05, $SeO_2$ 0.05, FeO 0.04, NiO 0.05, and CoO 0.04. Matrix corrections of Armstrong-Love/Scott φ(ρz) (Armstrong, 1988) and Henke MACs were used for data reduction. The instrument ran PeakSite v6.2 software for microscope operation and 'Probe for EPMA' software for all data acquisition and processing.

Laser ablation inductively coupled plasma mass spectroscopy (LA-ICP-MS) was utilized to quantitatively determine the concentration of trace elements dissolved in anode copper. Ten sub-samples were analysed, including representative samples in different orientations relative to the cooling face. Analysis spots were a consistent 38 μm in diameter, taking great care to avoid any visible inclusions. LA-ICP-MS trace element analysis was undertaken using a RESOlution-SE 193 nm excimer laser (Applied Spectra, USA) coupled to an Agilent 8900x quadrupole ICP-MS at Adelaide Microscopy, The University of Adelaide.

The suite of masses measured comprised twenty-three measured isotopes. Dwell times in ms and average minimum limits of detection (mdl, in ppm), are given in brackets. These are: $^{27}$Al (20, 1); $^{34}$S (20, 490); $^{53}$Cr (20, 1.2); $^{55}$Mn (20, 0.5); $^{56}$Fe (20, 6); $^{59}$Co (20, 0.02); $^{60}$Ni (20, 0.05); $^{65}$Cu (5, 2); $^{66}$Zn (20, 4); $^{75}$As (20, 0.4); $^{77}$Se (20, 3); $^{107}$Ag (20, 0.01); $^{118}$Sn (20, 0.2); $^{121}$Sb (20, 0.1); $^{125}$Te (20, 0.5); $^{137}$Ba (20, 0.001); $^{195}$Pt (20, 0.2); $^{197}$Au (20, 0.01); $^{204}$Pb, $^{206}$Pb, $^{207}$Pb and $^{208}$Pb (all 20, 0.04); and $^{209}$Bi (20, 0.025). Quantitative data were calculated by normalising the sum of all metallic cations to 100 %, with the copper metal (av. 99.9 % purity on average). The reference glass GSD-1G (US Geological Survey) served as a primary standard, with the STDGL3 lithium-borate-based glass reference material (Belousov et al., 2023) used a secondary standard. Nearly 500 spot analyses were found to be free of inclusions and comprise the dataset reported below. All laser spots deemed to strike an inclusion during ablation was not included in the calculation of concentration data.

A nanoscale element map was generated on a cut extracted by focussed ion beam scanning electron microscope (FIB-SEM) using an ultra-high resolution, probe-corrected, FEI Titan Themis instrument operated at 200 kV and equipped with a scanning transmission electron microscopy (STEM) energy-dispersive spectroscope (EDS) detector.

## 4. Results

### 4.1. Bulk composition of anode

Concentration data for elements of particular interest (in ppm) are given in Table 1. Alongside means and standard deviations for the full sample suite (n = 249), data for sub-sample C6, investigated at the micron-scale below, are given, together with data for its four closest neighbours (B6, C5, C7 and D6; Fig. 2B). Box-and-whisker plots showing element distributions for ten key elements in the full suite of 249 samples are shown as Fig. 3.

### 4.2. LA-ICP-MS analyses of copper

To evaluate the concentrations of elements dissolved in copper, LA-ICP-MS trace element analysis was conducted by placing randomly spaced laser spots on areas free of visible inclusions and at a distance from grain margins in ten representative polished blocks (Fig. 4). Data statistics are summarised in Table 2. The full dataset comprises 474 spot analyses from ten polished anode fragments and indicates that most

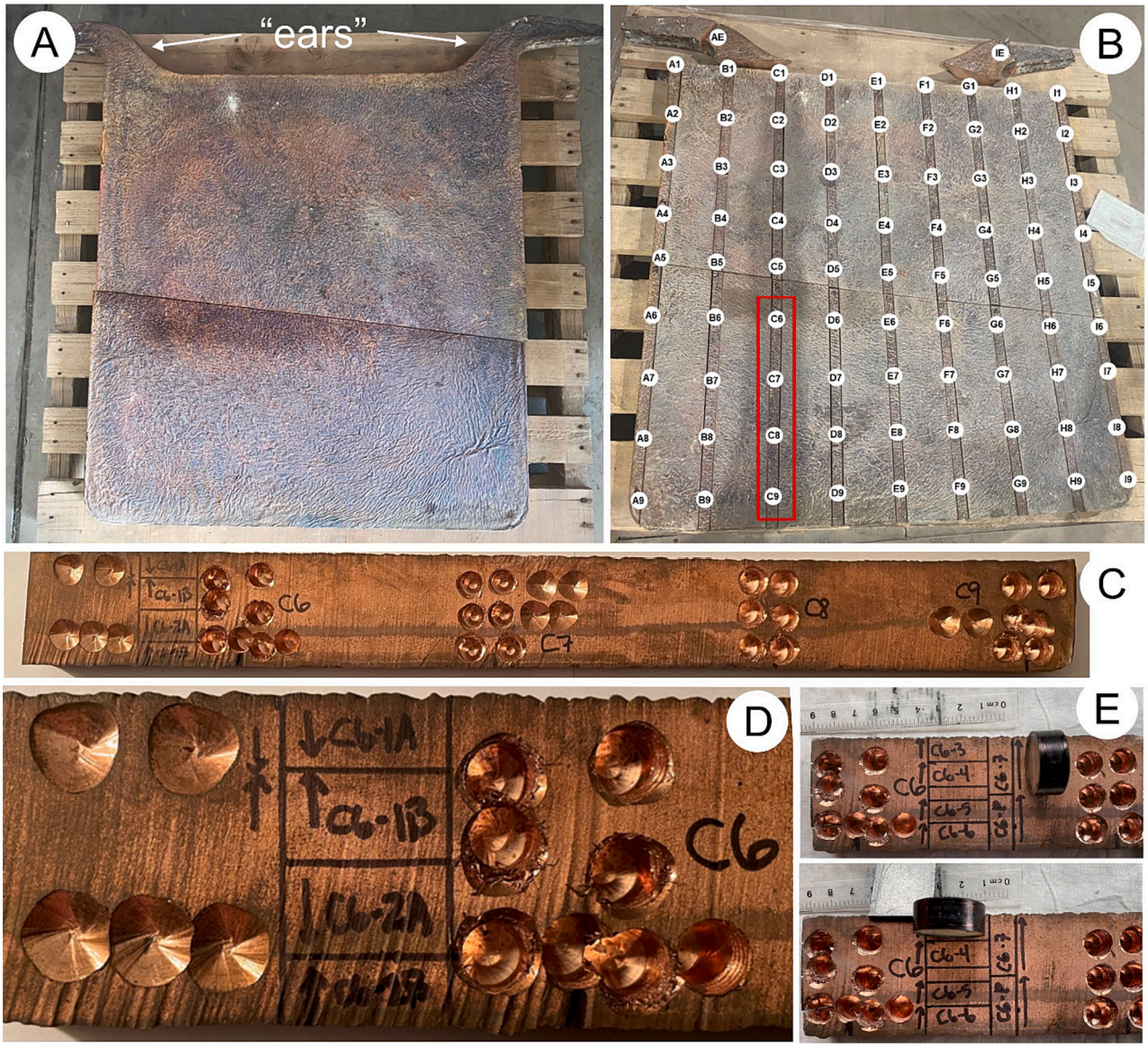


**Fig. 2.** Photographs illustrating (A) entire anode, including "ears", (B) superimposed grid of samples for assay, (C) cross-section of anode showing drilled-out strip sub-samples C6-C9 (red box on B), (D) detail of sample location C6 showing extraction of fragments for microanalytical study. The anode surface exposed to air (cold face) is on the top of image D, the anode bottom – surface in contact with casting mould – is at the bottom. The mounted and polished fragments C6-1A/B and C6-2A/B face one other. (E) Location and orientation of sub-samples C3-C8. Note that C3-C6 are parallel to surface exposed to air whereas C7 and C8 are cut perpendicular. (For interpretation of the references to colour in this figure legend, the reader is referred to the web version of this article.)

elements are reasonably evenly distributed throughout the copper, with relatively low standard deviations relative to concentration means (e.g., Au and Ni). Some elements, notably As, Sb and Bi, show greater variation than others with a larger proportion of outliers (Fig. 5). Bismuth, Pb, and Te display some of the highest standard deviations relative to the mean; Ni the lowest. The greater variation of these elements possibly relates to the ablation of nanoscale inclusions at depth, as will be discussed below.

Examination of time-resolved downhole LA-ICP-MS profiles shows that the Cu signals are quite noisy due to inherent poor ablation and potential melting. Profiles suggest, however, that although ~ 94 % of the analytical spots display smooth signals for trace components during ablation (Fig. 6A-D) a minority do not. The latter have signals suggestive of sub-micron-scale inclusions (Fig. 7). The association of elements (e.g., Pb-Bi and Co-Ni-Sn) in these smallest inclusions, invisible in optical image, matches those identified as discrete species in the larger (micron-scale) inclusions. Among the more common inclusions are ultrafine inclusions in which simultaneous spikes are observed in the signals for Fe, Co, Ni, and Sn (Fig. 7A, B), Pb alone, or Pb and Bi (Fig. 7C, D). Narrow spikes are observed in the Ag signal in several other profiles (Fig. 7E, F). A limited number of modest spikes in single-element signals were also seen, notably As and Au, although we acknowledge that these may be artefacts generated during ablation due to remobilisation of previously ablated material and often interpreted as signal noise rather than inclusions. In contrast, no small spikes were observed in the downhole signals for Sb, Se or Te. Anomalous signals for these elements were only seen where larger inclusions were intersected at depth (Fig. 7G). Interestingly, the signals for Ag and Au remain relatively flat as these larger inclusions are ablated. Segments of the downhole ablation profiles containing spikes, both large and small, were not integrated to obtain the data in Table 2.

The data in Table 2 confirm that a proportion of each impurity element occurs within copper metal but that the dissolved fraction measured in copper metal by LA-ICP-MS relative to the mean

**Table 1**
Assay data for bulk anodes, based on 269 samples (data in ppm).

| | Au | Ag | As | Bi | Co | Ni | Pb | Sb | Se | Sn | Te |
|---|---|---|---|---|---|---|---|---|---|---|---|
| All samples (n = 247) | | | | | | | | | | | |
| Mean | 31.2 | 174 | 1279 | 202 | 10.8 | 195 | 93.6 | 211 | 218 | 10.8 | 73.7 |
| S.D. | 0.60 | 6.4 | 41.1 | 9.4 | 1.67 | 5.9 | 6.3 | 8.2 | 10.8 | 0.63 | 3.4 |
| Sub-sample C6 and adjacent sub-samples | | | | | | | | | | | |
| C6 | 31.1 | 175 | 1273 | 199 | 12 | 200 | 93 | 219 | 232 | 11 | 77 |
| B6 | 31.6 | 181 | 1290 | 205 | 10 | 200 | 96 | 216 | 228 | 11 | 79 |
| C5 | 31.4 | 172 | 1341 | 209 | 10 | 193 | 95 | 206 | 226 | 11 | 75 |
| C7 | 32.0 | 180 | 1286 | 204 | 9 | 195 | 110 | 221 | 234 | 11 | 76 |
| D6 | 31.3 | 180 | 1300 | 200 | 9 | 198 | 100 | 208 | 245 | 10 | 76 |

Minimum detection limits (in ppm): Au 0.005, Ag 5, As 5, Ba 0.5, Bi 1, Co 1, Ni 20, Pb 50, Sb 5, Se 50, Sn 2, Te 5.
Mean concentrations of other minor elements (ppm unless otherwise stated): Ca (0.014%), Fe (0.02%), Ga (0.16), Ge (0.6), In (0.09). Li (4.6), S (0.017%), Si (0.02%), Sr (0.53), Th (0.09), Ti (0.006%), $U_3O_8$ (0.5).
Concentrations of the following elements were consistently below their respective minimum limits of detection (in brackets, ppm unless otherwise stated): Al (0.01 %), Ba (20, with a single analysis of 22 ppm), Be (0.5), Cd (0.2), Ce (20), Cr (20), Cs (0.05), Dy (0.05), Er (0.05), Eu (0.05), Gd (0.05), Hf (0.1), Ho (0.02), K (0.01 %), La (10), Lu (0.02), Mg (0.01 %), Mn (0.005 %)Mo (1), Na (0.01 %), Nb (0.1), Nd (0.1), P (0.01 %), Pr (0.05), Rb (0.1), Re (0.02), Sc (2), Sm (0.05), Ta (0.1), Tb (0.02), Tl (0.2), Tm (0.05), V (5), W (1), Y (0.5), Yb (0.05), Zn (50), Zr (1).
Analytical methodologies: Fire-assay / optical emission spectroscopy (Au), Four-acid-HBr / mass spectroscopy (Ag, As, Bi, Cd, Co, Ge, In, Li, Ni, Pb, Re, Se, Te, Tl, Zn), four-acid-HBr optical emission spectroscopy (S), lithium borate fusion / optical emission spectroscopy (Al, Ca, Cr, Fe, K, Mg, Mn, Na, P, Sc, Si, Ti), lithium borate fusion / mass spectroscopy (Ba, Be, Ce, Cs, Dy, Er, Eu, Ga, Gd, Hf, Ho, La, Lu, Mo, Nb, Nd, Pr, Rb, Sb, Sm, Sn, Sr, Ta, Tb, Th, Tm, $U_3O_8$, V, W, Y, Yb, Zr).

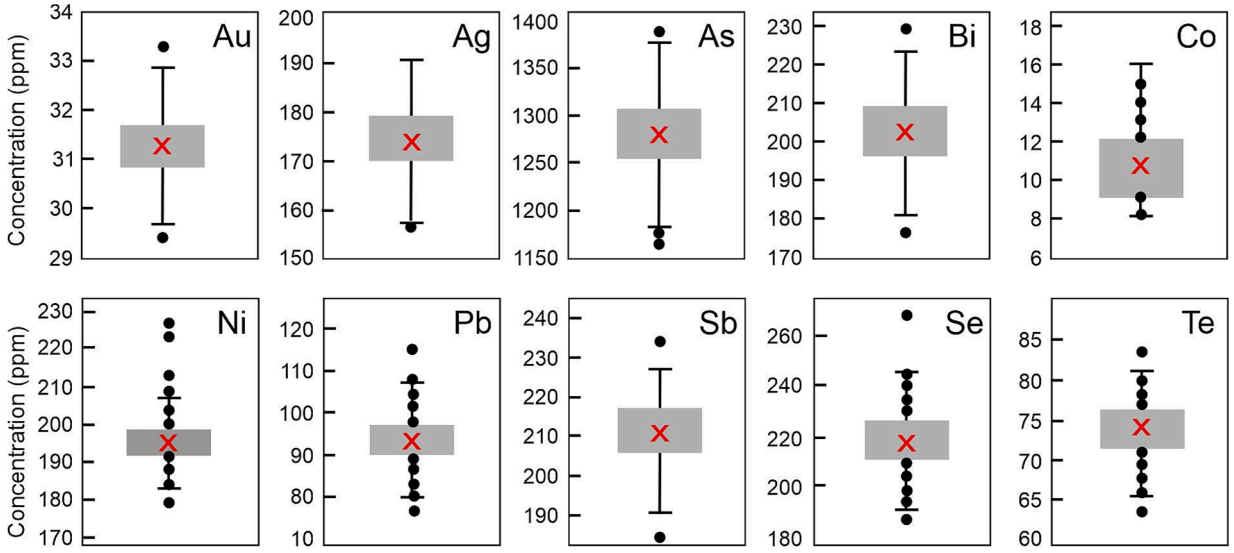


**Fig. 3.** Box and whisker plots for ten selected elements in copper anodes (mean – red cross, 95% confidence level in box, values in ppm), showing variation in measured concentrations. Note narrow range of measured values for all elements. (For interpretation of the references to colour in this figure legend, the reader is referred to the web version of this article.)

concentration determined by bulk assay (Table 1) varies significantly from element to element. This fraction ranges from as little as 9.3 % for Pb, 13.7 % for Bi, 14.1 % for Te, 25.1 % for Se, 29.4 % for Sn, through Sb (34.9 %), As (55.3 %), Au (57.0 %), Ag (61.8 %), to Co (67.0 %). Only in the case of Ni, is ~ 100 % of the metal dissolved in copper metal.

Data processing to obtain the mean values in Table 2 involved removal of 30 points where the downhole LA-ICP-MS profile indicated the presence of sub-microscopic inclusions. If these data had been included, the mean concentrations of all elements in copper would be greater, albeit also with a larger standard deviation on that mean. Similarly, the calculated proportion of the total within copper would also be higher. Thus, the mean concentrations of elements as given in Table 2 is best considered a minimum, as it ignores elements still 'contained' in copper metal although as sub-microscopic inclusions rather than in solid solution.

Twenty additional laser spots were placed on visible multiphase inclusions within copper. The resultant data cannot be regarded as quantitative given that these inclusions contain two or more chemically different phases, as well as the unknown volume of the inclusion, which is anyway exceeded by the ablated volume. Nevertheless, some valuable insights are obtained. With the exception of Ni, all elements of interest, i.e., Au (tens of ppm), Ag (hundreds of ppm), As, Bi, Co, Pb, Sb, Se, Sn, and Te, are present at concentrations several times higher than in copper in clean areas. Nickel concentrations are, however, lower, confirming the conclusion that nickel is almost exclusively restricted to solid solution in copper. We also note measurable "concentrations" of Fe (up to hundreds of ppm) and even Zn (3–8 ppm). Interestingly, both Ag and Au show comparatively smooth depth profiles across different inclusion species in marked contrast with other elements (Fig. 8).

Correlation analysis of the LA-ICP-MS dataset shows some useful trends (Fig. 9). These include correlations that might be expected from geochemical affinity, such as between Ag and Au ($r'$=0.88; Fig. 9A), Pb and Bi ($r'$=0.89; Fig. 9B), Co and Ni ($r'$=0.85; Fig. 9C), Sb vs. As ($r'$=0.97; Fig. 9D), or Te vs. Se ($r'$=0.97; Fig. 9E). Other strong correlations are suggestive of the element associations observed together as compounds within the visible inclusions, notably between Bi and As ($r'$=0.93; Fig. 9F), Ag and Se ($r'$=0.87, Fig. 9G) or Sn vs. Sb ($r'$=0.90, Fig. 9H). In fact, there is a broad correlation among most elements, again raising

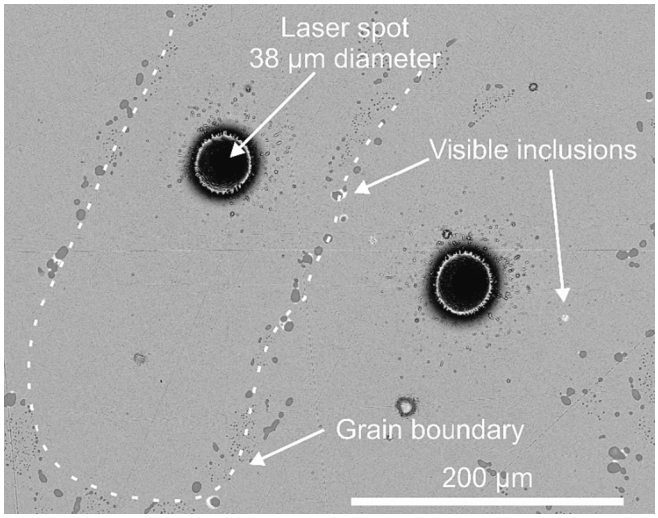


**Fig. 4.** BSE image showing representative example of polished sample surface with location of laser spots relative to visible inclusions and copper grain margins. Dark inclusions are cuprite, brighter inclusions contain Bi, As, Pb etc. Small dark spots around laser spots are splatter from ablation.

questions about how they are incorporated in copper metal – true dissolution (solid solution), or – at least in part, as semi-regularly dispersed nanoparticles containing two or more similar or otherwise compatible elements? A plot of Sn vs. Co ($r'$=-0.64, Fig. 9H) shows a moderately strong negative correlation, which is at odds with the common co-occurrence of these two low-abundance elements.

### 4.3. Inclusion phases

Inspection of anode samples in reflected light and low-magnification SEM imaging show a small number of relatively large (>100 μm) pores throughout the sample. Cuprite, $Cu_2O$, is the most abundant inclusion phase in the anodes, occurring as relatively large (10–50 μm-sized), typically (sub)-rounded grains at boundaries of copper crystals. Cuprite can be seen as oriented splays generated via degassing during cooling (Fig. 10A) but is more commonly seen as inclusions, which are often arranged as networks at the margins of copper grains roughly 100 μm apart (Fig. 10B, C). Electron probe microanalysis of six representative cuprite inclusions across multiple samples showed that only the following elements were present at concentrations above minimum detection limits: BaO 0.05–0.06 wt%, $Al_2O_3$ 0.07 wt%, $As_2O_3$ 0.13 wt%, $SeO_2$ 0.16–0.22 wt%.

Inclusions of other impurity components are bright on the BSE images and either tied to cuprite and networks of cuprite inclusions (Fig. 10C) or isolated within copper grains, occasionally showing clustering (Fig. 10D). Most impurity inclusions are (sub)-rounded to elongate in shape and typically in the size range 1–6 μm diameter, rarely up to as large as ~ 12 μm. Inclusions dominated by Bi, Pb, and other metals commonly cluster around the cuprite inclusions (Fig. 10E). Many inclusions are multiphase and may contain grains of cuprite that display either euhedral or subhedral morphology (Fig. 10E, F), appears as skeletal, herring-bone-like microcrystals (Fig. 10G) or tiny worm-like grains (Fig. 10H). Each multiphase inclusion (Fig. 10I-K) displays a unique bulk composition and proportion of different phases reflecting the composition of the trapped melt.

The morphologies, degree of complexity, and phases identified in each multiphase inclusion vary significantly. There are broadly three distinct types, as illustrated in Fig. 10K: Cu-Bi-(As-Sb)-oxides of wide-ranging composition and degree of crystallinity surrounded by a narrow halo of $Cu_{2+x}$(Se,Te); Cu-Bi-As-oxides and the $Cu_{2+x}$(Se,Te) phase with worm-like cuprite; and glassy Pb-bearing Cu-Bi-As-oxides associated with cuprite, sometimes also with a halo of $Cu_{2+x}$(Se,Te). A detailed treatment of inclusion phases in anodes, their textures, mutual relationships, and composition, calculated stoichiometry, crystallinity, and where applicable, also crystal structure, will be presented and amply illustrated in a future publication.

Inclusion characterization and microanalysis is challenging in that species are often intergrown with one another at the sub-micron scale, appear clearly compositionally heterogeneous on BSE images, or are too small (>1x1x1 μm) to obtain reliable compositional data. These challenges are compounded by some grains being extremely thin at the section surface (effectively transparent to the electron beam; Fig. 10E), often poorly crystalline or amorphous, readily damaged during section preparation and polishing, highly beam sensitive, and in some cases, unstable or partially decomposed.

Acquisition of reliable electron probe data for the Cu-selenide phase was plagued by interference from associated phases but enabled confirmation of $Cu_{2+x}$(Se,Te) stoichiometry (x = 0.2–0.25) recognised from several hundred EDS analysis. Probe data also confirmed Se/(Se + Te) ratios of ~ 0.73–0.77 (atom. basis), as well as the presence of ~ 0.5 % wt. S, 0.5–0.8 wt% Ag, and 0.7–1.5 wt% Au.

To further support the argument that the micron-scale inclusions have complex sub-structures and can also host a wider range of impurity elements beyond those contained in the main identifiable phases, we show, as Fig. 11, a series of nanoscale element maps of a representative ~ 7 μm-diameter multi-phase inclusion. These chemical maps are of a thinned foil extracted *in-situ* from the polished anode surface by FIB-SEM (Fig. 11A-C). The inclusion comprises cuprite, $Cu_2$(Se,Te), and Cu-Bi-As-(Sb)-oxide. The element maps (Fig. 11D) show cuprite, $Cu_{2+x}$(Se,Te), and a Cu-Bi-As-(Sb)-oxide as main phases occurring as sub-grains that extend in size well below 1 μm in diameter, but also sub-grains of both $Cu_{2+x}$(Se,Te) and Cu-Bi-As-(Sb)-oxide that appear relatively enriched in silver.

## 5. Discussion

### 5.1. Elements dissolved in copper metal

The concentrations of minor elements dissolved in copper metal have been determined by LA-ICP-MS spot analysis on areas without visible inclusions. LA-ICP-MS offers the necessary sensitivity at low ppm-level concentrations yet requires analysis of a relatively large sample volume (thousands of $\mu m^3$). The mean measured values given in Table 2 are therefore after removal of any analysis suggestive of discrete nanoscale inclusions. Nevertheless, the resultant dataset indicates relative homogeneity at the scale of the sub-samples. Measured concentrations of

**Table 2**
LA-ICP-MS trace element data for copper (n = 474, data in ppm).

| | Au | Ag | As | Bi | Co | Ni | Pb (tot) | Sb | Se | Sn | Te |
|---|---|---|---|---|---|---|---|---|---|---|---|
| Mean | 17.8 | 107 | 707 | 27.8 | 7.4 | 209 | 8.8 | 73.6 | 54.6 | 3.2 | 10.5 |
| S.D. | 3.0 | 40.5 | 352 | 27.0 | 1.5 | 25 | 6.2 | 44.5 | 30.6 | 1.0 | 7.2 |
| Max | 29.3 | 295 | 1931 | 165 | 12.5 | 262 | 96.3 | 253 | 149 | 8.3 | 46.8 |
| Min | 12.4 | 61.7 | 281 | 2.1 | 3.7 | 146 | 2.2 | 18.3 | 10.8 | 1.1 | 1.2 |

Concentrations of Al, Cr, Cr, Mn, Fe, Zn, Ba, and Pt were consistently below their respective minimum limits of detection. Pb(tot) represents the sum of measured $^{204}Pb + ^{206}Pb + ^{207}Pb + ^{208}Pb$.

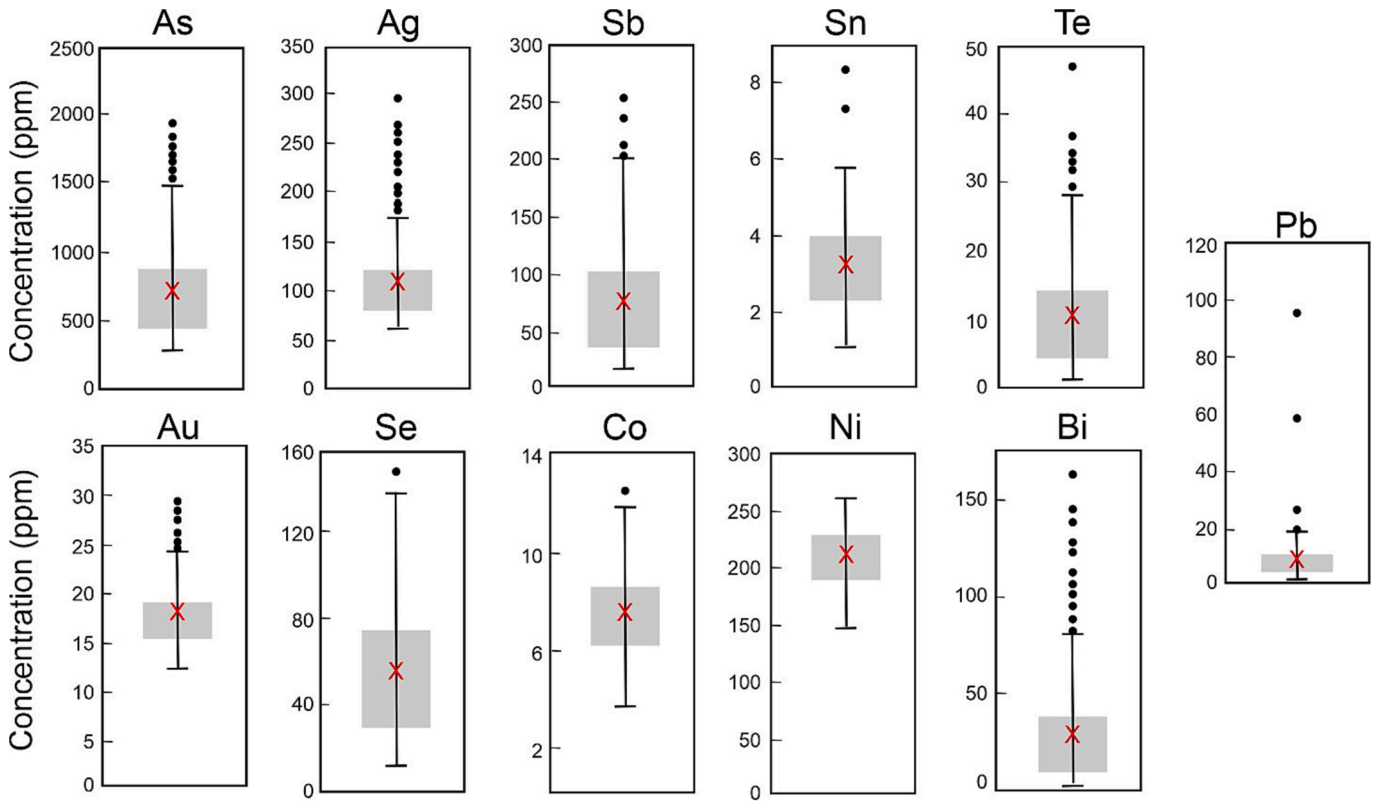


**Fig. 5.** Box and whisker plots showing LA-ICP-MS parts-per-million trace element concentration data for anode copper based on 474 spot analyses of inclusion-free areas. Mean concentration is given by the red cross and the 95% confidence level is indicated by the grey box. All analyses indicating sub-micron-scale inclusions on time-resolved downhole profiles were removed during processing. (For interpretation of the references to colour in this figure legend, the reader is referred to the web version of this article.)

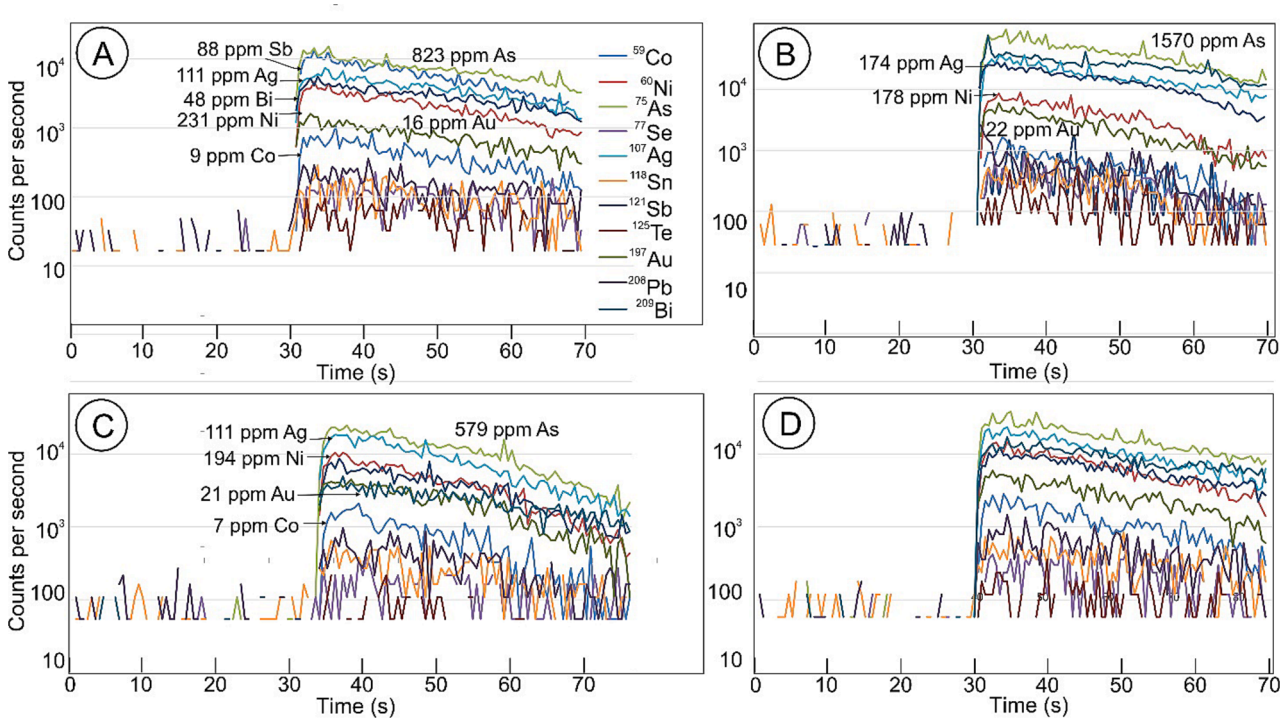


**Fig. 6.** LA-ICP-MS time-resolved downhole profiles showing moderately smooth signals for elements of interest and integrated ppm concentrations for selected elements on A-C. Sample/spot numbers are C6-1A-E3 (A), C6-1A-J2 (B), C6-2A-A1 (C), and C6-7-B1 (D).

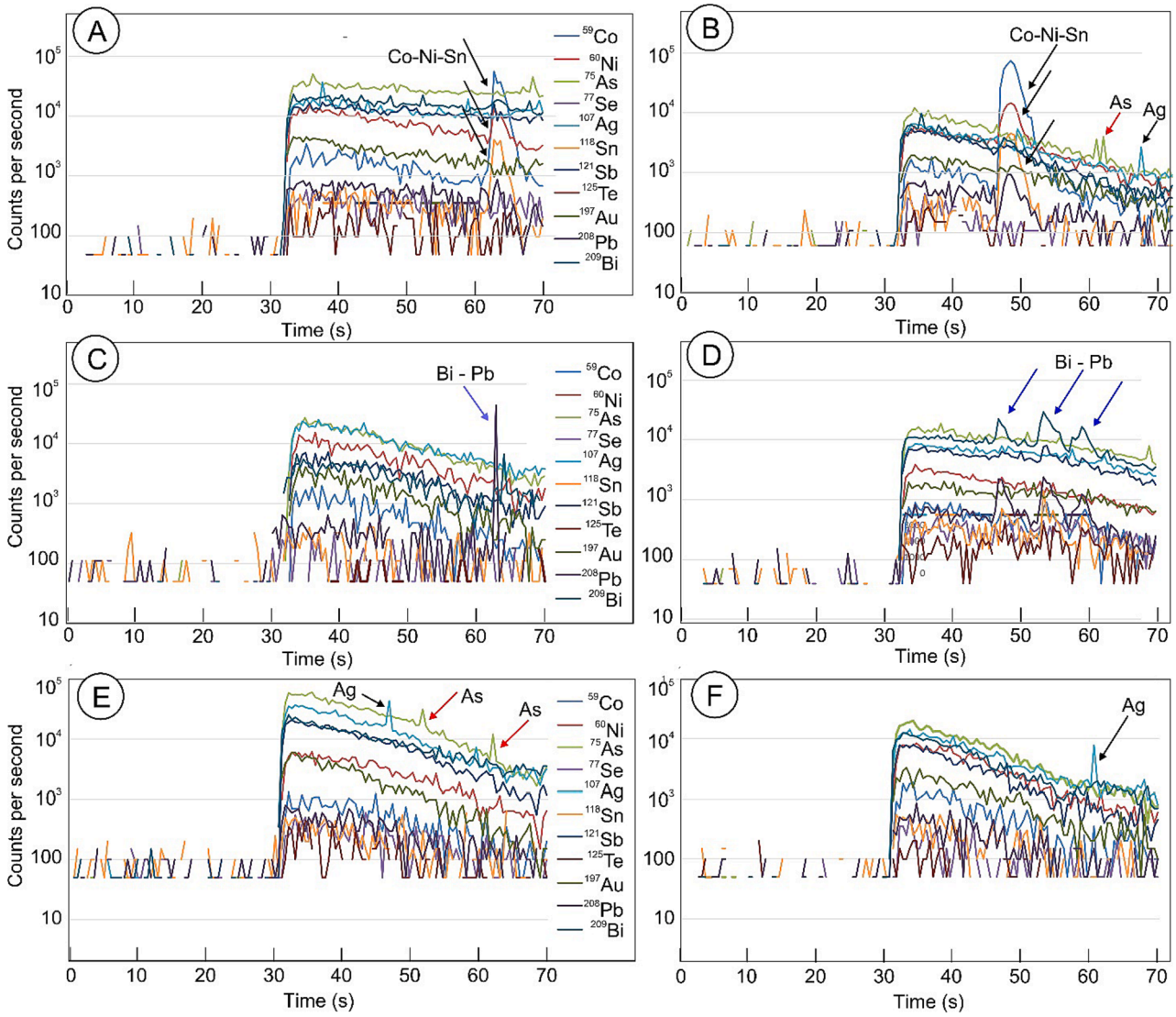


**Fig. 7.** LA-ICP-MS time-resolved downhole profiles showing small spikes suggestive of different species of sub-microscopic inclusions as labelled. Sample/spot numbers are C6-1A-F4 (A), C6-2A-A4 (B), C6-1A-H1 (C), C6-1A-J5 (D), C6-1B-C1 (E), and C6-1B-D4 (F).

minor elements in copper are well below established solubility limits for common minor elements in copper, e.g., 4.9 % for Ag (Subramanian and Perepezko, 1993), or 8.5 % for Bi (Chakrabarti and Laughlin, 1984). Solubility limits for Te are several orders of magnitude lower and decrease rapidly during cooling, leading Chen and Dutrizac (1993) to propose a degree of metastable solid solution. Most elements show a reasonably tight distribution around the respective mean. Likewise, the distributions of minor elements across the entire anode appears

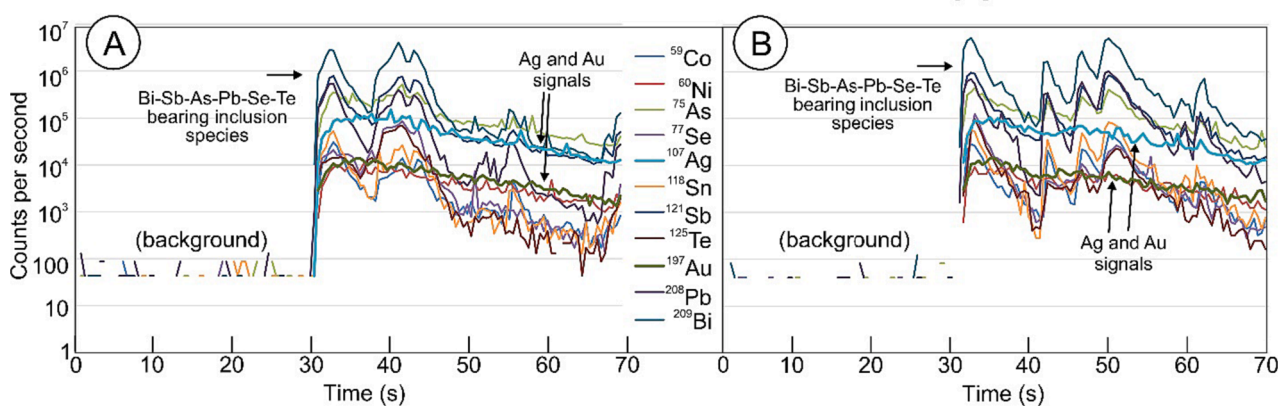


**Fig. 8.** Representative time-resolved downhole LA-ICP-MS profiles through visible multiphase inclusions. Note relatively smooth signals for Au and Ag in contrast with other elements. Sample/spot numbers are C6-1B-incl4 (A) and C6-1B-incl19.

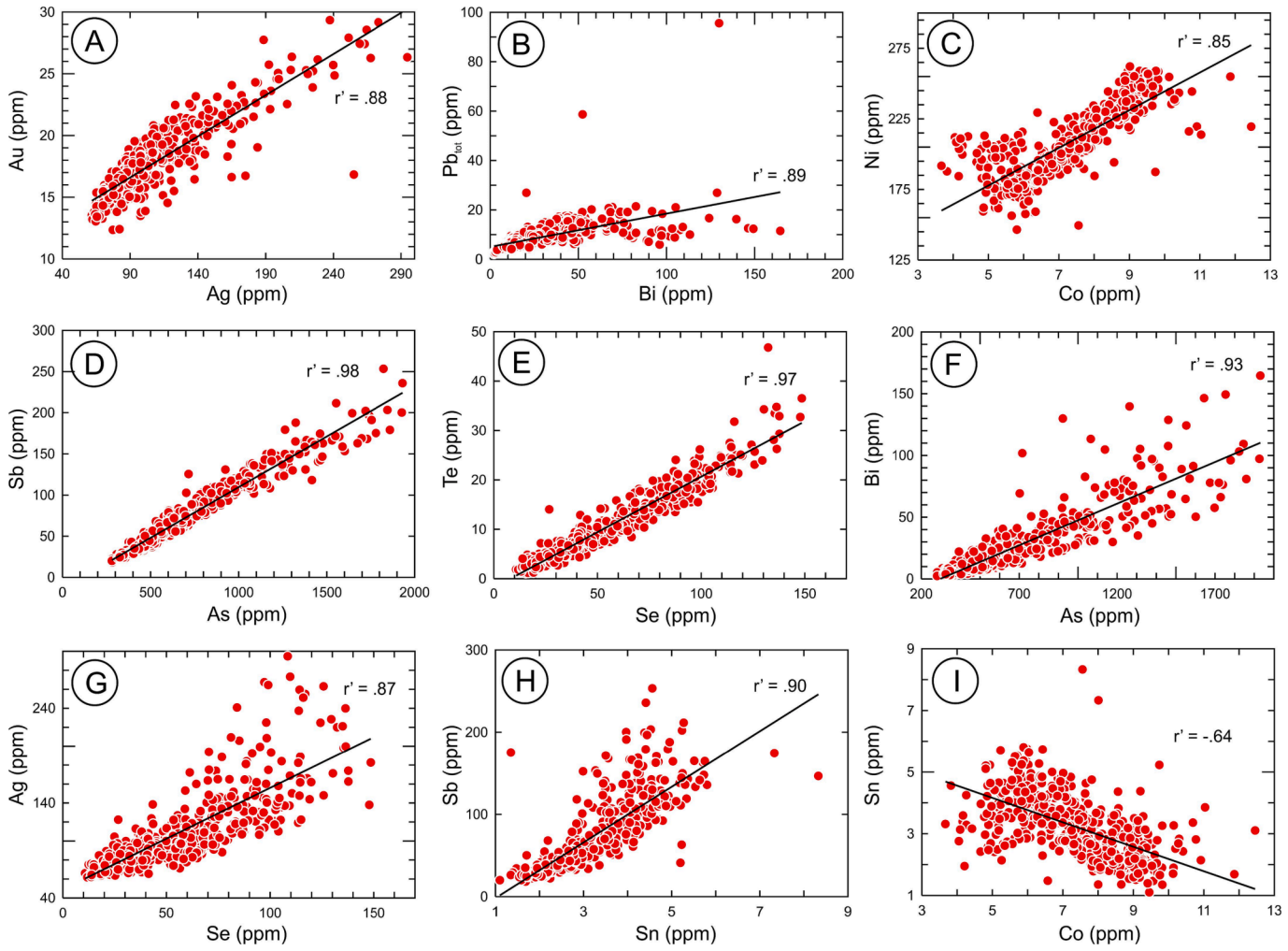


**Fig. 9.** Selected binary plots showing correlation trends among trace element pairs in copper anode (474 spot analyses, inclusion-free areas only).

homogeneous, irrespective of location or orientation, consistent with findings elsewhere (e.g., Wenzl et al., 2008).

Focussing solely on these data and ignoring information contained in the excluded LA-ICP-MS analyses nevertheless conceals the true nature of minor elements deemed to be contained within copper metal. We draw attention to outlier concentrations, likely an indication of sub-micron inclusions especially in the case of As, Te, Ag, Au, and Bi (Fig. 5), the population of spot analyses containing sub-micron-scale inclusions (Fig. 7), and the surprisingly good correlations among all elements (Fig. 8). Taken together, this evidence favours a distribution model in which true solid solution is accompanied by non-randomly located inclusions far smaller than those shown in Fig. 9 and thus effectively invisible on BSE images. We also speculate that although the distribution of minor elements is reasonably homogeneous across an entire anode, it may not be so at the scale of an individual copper grain. It is reasonable to suggest that trace element concentrations, and perhaps also the abundance and/or size of inclusions, increases towards grain margins, where the larger inclusions occur, as a function of temperature gradient-driven diffusion during cooling. Such a hypothesis would require empirical confirmation using a suitable method to visualise subtle variation in ppm-level concentrations at the micron-scale.

Unequivocally distinguishing true solid solution from nanosized inclusions, or establishing the relative proportions of the two modes of occurrence where they co-exist, is a challenge frequently faced since adoption of LA-ICP-MS as the standard method to obtain reliable quantitative concentration data for trace elements in mineral matrices. A partial resolution of this question can be achieved by coupling micron-scale LA-ICP-MS microanalysis with nanoscale study of the same samples, as the present authors recently found when attempting to resolve the nature of "invisible gold" in pyrite from Olympic Dam (Ehrig et al., 2023). In another attempt to reconcile the presence of inclusions from LA-ICP-MS data, Cook et al. (2022) related the estimated number of nanoinclusions of specific size (from nanoscale imaging) that would be needed to give a certain concentration. This exercise, focussing on monazite inclusions in a hematite matrix, showed that the number of inclusions observed, their average size, density and chemistry, could be reconciled with measured concentrations of rare earths in LA-ICP-MS spot analyses.

### 5.2. *Partitioning between solid solution and inclusions*

In the Olympic Dam anodes, the budgets for each element of interest are split between copper metal and impurity inclusions. Nearly 100 % of all Ni is contained in copper metal even though we note measurable concentrations of Ni within (scarce) Sn-bearing oxides. Inclusion hosts for Se and Te are almost exclusively $Cu_{2+x}$(Se,Te). Although nanoscale inclusions are seen as spikes on the LA-ICP-MS depth profiles, we have not observed discrete inclusions of phases containing essential Au and Ag (in metallic form or as compounds with Se, Te, or other elements) at the micron-scale. Instead, EDS and EPMA data show that the precious metals occur in solid solution within $Cu_{2+x}$(Se,Te) at low to moderate concentrations, and as confirmed by LA-ICP-MS analysis of the larger multi-component inclusions, probably, also at grain boundaries between selenides, arsenates, and cuprite etc.

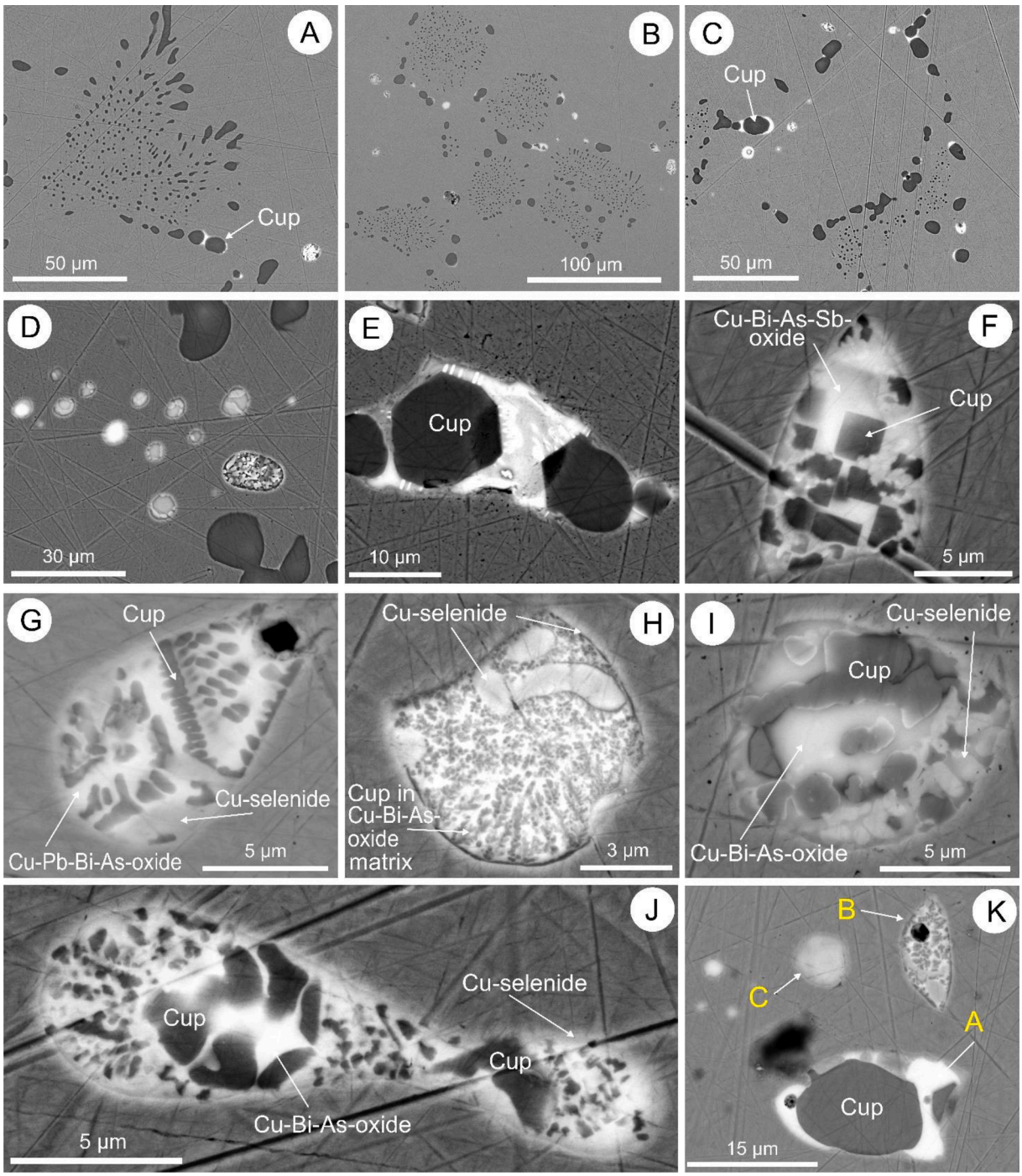


**Fig. 10.** BSE images showing overall structures within copper anodes. (A) Splay-like arrangement of small cuprite grains (dark, Cup) originating from degassing during cooling (sample C6-3). (B, C) Circular to oval networks of interconnected cuprite grains (dark colour) located at copper boundaries (samples C6-3, C6-1B). Brighter spots are impurity inclusions containing heavier elements, As, Bi, Sb, Ag, Pb, etc. (D) Atypically dense cluster of micron-sized inclusions, mostly Cu-Bi-As- and Cu-Pb-Bi-As-oxides with narrow haloes of Cu-selenide (sample C6-7). (E) Larger sub-idiomorphic cuprite enclosed by fine sub-micron-scale intergrowth of Cu-Pb-Bi-As-oxide and Cu-selenide (sample C6-3). (F) Idiomorphic cuprite within impurity inclusion largely composed of Cu-Bi-As-Sb-oxide (sample C6-1A). (G) Cuprite microcrystals in a skeletal herring-bone arrangement within Cu-Pb-Bi-As-oxide and marginal Cu-selenide (sample C6-1A). (H) Fine, microcrystals of cuprite within multiphase impurity inclusion as labelled (sample C6-1A). (I) Composite inclusion as labelled (sample C6-1B). (J) Larger, elongate impurity inclusion containing cuprite grains of different sizes, Cu-Pb-Bi-As-oxide, and thin outer rim of Cu-selenide (sample C6-2A). (K) Cluster of impurity inclusions of three distinct types: Pb-bearing phases associated with cuprite [yellow A], Cu-Bi-arsenate and selenide phase with worm-like cuprite [yellow B], and single phase Cu-Bi-(As-Sb) with narrow halo of $Cu_{2+x}$(Se,Te) [yellow C] (sample C6-2A). (For interpretation of the references to colour in this figure legend, the reader is referred to the web version of this article.)

Bismuth, As and Sb occur in the form of a diverse suite of crystalline oxides and other compounds with copper and with varying stoichiometry and compositions that range from Bi-rich (~70 wt% Bi) to Cu-rich, Bi-poor (<20 wt% Bi). Some Bi-rich species are crystalline and correspond to stoichiometric $CuBi_2(As,Sb)O_6$. Tin, Co, and Fe occur within a more diverse range of compounds. Lead mostly occurs in Cu-Pb-As-Sb-Bi oxide inclusions.

A detailed description of these phases, based on observation and

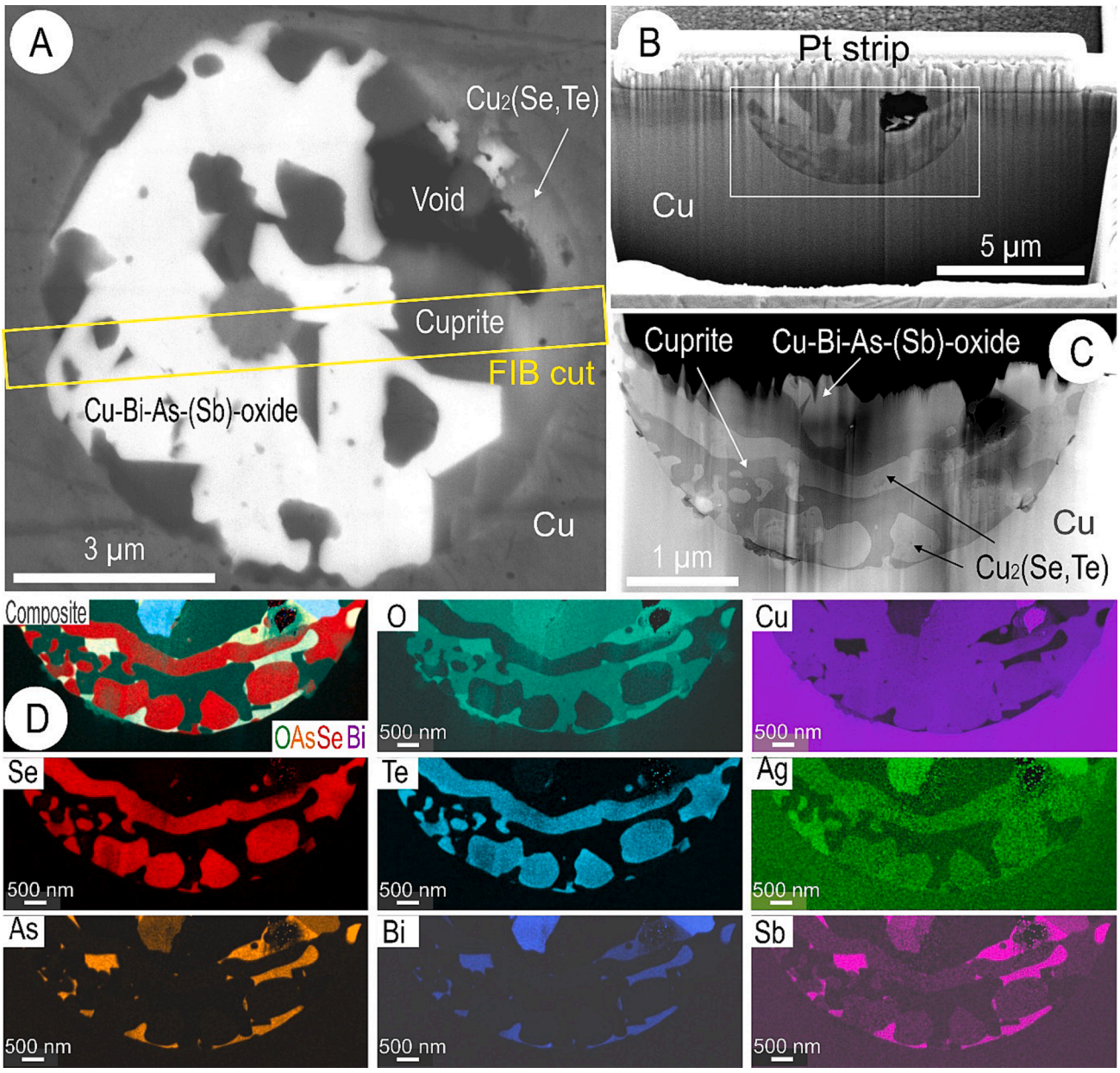


**Fig. 11.** (A) BSE image of representative multiphase impurity inclusion in anode (plan view) prior to FIB-cutting and thinning. Area of FIB cut indicated in yellow. (B) Image of vertical face of cut prior to extraction from sample. (C) Thinned foil showing distinct impurity phases as different grey shades. (D) STEM EDS element maps of extracted foil showing the range of compositions in a micron-scale multiphase inclusion. Cuprite is picked out in dark green on the composite map (top left of D) and on the oxygen map. $Cu_2$(Se,Te) and Cu-Bi-As-(Sb)-oxide are also readily picked out (for example, compare Se and As maps). Silver is not a major component of any phase but is elevated (i.e., brighter on Ag map) in some $Cu_2$(Se,Te) and Cu-Bi-As-(Sb)-oxide subgrains. (For interpretation of the references to colour in this figure legend, the reader is referred to the web version of this article.)

analysis of several thousand individual inclusions, will be presented elsewhere, allowing further assessment of inclusion chemistry, element distributions, and their mutual relationships at the nano- to micron-scales. The $Cu_{2+x}$(Se,Te) phase is crystalline and demands further investigation at the nanoscale to resolve crystal structure and relationship, if any, with known mineral species in the systems Cu-Se, Cu-Te, and Cu-Se-Te. Together with new experimental and *ab-initio* data (e.g., Ge et al., 2023), a mineralogy-inspired approach using complementary microanalytical methods, like that used here, can make a significant contribution to minor element deportment during smelting-to-electrolysis.

### 5.3. Comparison with other operations

There is less published data on the impurities in anodes than in refinery slimes. This is largely because almost all copper produced by smelting is sent for electrorefining to remove impurities under the widely accepted yet flawed assumption that anodes and their contained impurities dissolve completely in electrolyte and therefore that the speciation of impurity elements in the leached anode is of only marginal significance to efficient electrolysis. Anodes need to meet strict quality standards, including a uniform distribution of impurities and ideally coarser grain size of copper to prevent anode passivation (Wenzl et al., 2008). These authors also point to temperature gradients between the margin-to-mould and margin-to-air during the anode casting process, which can lead to a degree of heterogeneity with respect to both

impurity distribution and grain size, although such features are not observed in the present study. As shown for Te (Chen and Dutrizac, 1990b), impurity speciation can have a major impact on reaction at the anode interface, and implicitly on efficacy of electrorefining.

The mineralogy of copper anodes from different operations varies with feedstock and smelting parameters, generating anodes with highly variable concentrations of impurities and proportions of different impurity phases. Nevertheless, mineralogical investigation of anodes from some of the world's largest operations shows certain generalities. Most documented examples point to cuprite as the most abundant inclusion species, typically occurring as spheroidal inclusions, 1 to 20 μm in size, located at copper grain boundaries (Chen and Dutrizac, 1990b; Beauchemin et al., 2008). Cuprite is associated with Cu-selenides and various Cu-Bi-As- and Cu-Pb-As-Sb-Bi oxides comparable with those shown here. Like the Cu-selenides observed by us, analogues from other smelters (Chen and Dutrizac, 1990b) contain both Ag (~1%) and Te (5–10 %), and also like in our study, Ag-selenides are not observed. Other similarities include the almost ubiquitous co-occurrence of Cu-selenides and Bi-As-oxides, a feature of relatively Bi-(As)-rich anodes (Chen and Dutrizac, 1990b). High impurity contents in anode, notably Pb, Ag, Ni, Sb, and Sn, are considered to make anodes more vulnerable to passivation (Mubarak et al., 2007). Moreover, the behaviour of As, Sb, and Bi during electrorefining and the partitioning of these elements between anode slimes and electrolyte will depend, at least to some extent, on how they occur in anode and whether complete dissolution is achieved.

Anode copper from Inco's Copper Cliff Copper Refinery (Chen and Dutrizac, 1988) also contained oxide and selenide inclusions, occurring mostly, although not exclusively, at copper grain boundaries. As in our case, almost all Ag, and most of the Ni, was found to be in solid solution, although some of the latter was present as euhedral sub-10 μm-sized crystals of NiO, perhaps reflecting the far higher bulk Ni content. Some Ni and Se were also measured in $Cu_2O$. As in our study, Pb-Cu-Bi oxides were observed in some of multiphase inclusions. In contrast, we did not observe any of the Cu-Ni-silicate or Ca-Cu-Ni-silicate inclusions identified in Copper Cliff anode.

Anodes from the Chuquicamata Division of Codelco-Chile were documented by Chen and Dutrizac (1991). Similar to our study, copper metal contained most of the Ag and a significant proportion of the As and Sb in solid solution. Inclusions of $Cu_2O$, $Cu_2Se$ and Cu–Sb–As oxide were noted. As in the present study, the $Cu_2Se$ was found to have a significant solid solution Te component, but in contrast to those studied here, the Chilean anodes contained $Cu_2Se$ inclusions carrying several wt. % sulphur. We can realistically infer that the small amounts of S we measure are substituted within the copper selenides, as indicated by studies elsewhere (e.g., Kanari et al., 2019).

A further example documented in the literature (Chen and Dutrizac, 2005) deals with anode copper from the La Caridad refinery of Mexicana de Cobre. As in our study, although some of the Pb, As, Sb, and Bi was present in solid solution in copper metal, the larger part occurred as complex Cu-Pb-As oxide and Cu-Pb-As-Sb-Bi oxide inclusions. The behaviour of Pb during electrorefining described from La Caridad resembles our own observations of anode slimes from Olympic Dam (Cook et al., 2024), whereby solid solution and inclusion-hosted Pb, As, Sb, and Bi dissolve, with Pb reacting with electrolyte to form crystalline $PbSO_4$ that occurs together with diverse Bi-As-Sb-(Sn)-oxides in the anode slimes.

## 6. Conclusions

Ten key conclusions are drawn from this study:

1. Comprehensive sampling and assaying of anodes show they are compositionally homogeneous within analytical error and that sampling of the anode ears can provide a reliable indication of bulk chemistry.
2. *In-situ* LA-ICP-MS trace element analysis provides information on metals contained in solid solution within copper metal. Some elements show greater variability and larger proportion of outliers than others. Arsenic is the most abundant impurity (1279 ppm), followed by Se, Sb, Bi, and Ni (all ~ 200 ppm). Silver and gold concentrations are 174 and 31.2 ppm, respectively.
3. Nickel occurs almost completely contained within copper metal. Other elements occur only partially in dissolved form, but proportions vary significantly from only ~ 9 % for Pb, 14 % for Bi and Te, 25 % for Se, 29 % for Sn, 35 % for Sb, 55 % for As, 57 % for Au, 62 % for Ag, and 67 % for Co.
4. The unexpectedly strong correlations between many trace element pairs raise the possibility that impurity distributions are not fully evenly distributed at the micron-scale. The same observation may also be interpreted as showing some of the higher measured concentrations reflect semi-randomly distributed nanoparticles rather than dissolution in copper (solid solution).
5. Some of the time-resolved downhole LA-ICP-MS profiles indicate the presence of sub-micron-scale inclusions bearing a comparable geochemical signature (e.g., Pb-Bi, Fe-Co-Sn) as species seen at the micron-scale in the larger inclusions. Laser spots placed on visible (micron-scale) inclusions, backed up by electron probe data, indicated that impurities such as Ag and Au that do not occur as discrete phases may still occur 'dissolved' within other inclusion phases and at grain boundaries in multiphase inclusions.
6. Impurity inclusions are located at copper grain boundaries or associated with cuprite. Most inclusions are multiphase and have a unique composition reflecting a small portion of trapped melt.
7. Cuprite, $Cu_2O$, is the most abundant inclusion species. Electron probe microanalysis did not reveal the presence of other impurity elements.
8. Impurity inclusions can be either crystalline (e.g., Cu-selenides, some Cu-Bi-arsenates, Sn-oxides) or amorphous (e.g. Cu-Pb-As-Sb-Bi oxide glasses)
9. Although mostly in copper metal, traces of Ag and Au are noted in Cu-selenides, which also contain subordinate Te. Impurity-hosted Bi, As and Sb typically occur in the form of oxide compounds with copper. Tin occurs as cassiterite and together with Co and Fe in a diverse range of oxide compounds. Lead mostly occurs as Cu-Pb-As-Sb-Bi oxide inclusions.
10. The distributions of impurity elements in Olympic Dam anodes closely resemble examples documented from other smelter operations. Differences in deportment and impurity species reflect the unique nature of each feedstock.

## CRediT authorship contribution statement

**Nigel J. Cook:** Writing – review & editing, Writing – original draft, Methodology, Investigation, Funding acquisition, Conceptualization. **Kathy Ehrig:** Writing – review & editing, Writing – original draft, Resources, Methodology, Investigation, Funding acquisition, Conceptualization. **Cristiana L. Ciobanu:** Writing – review & editing, Writing – original draft, Methodology, Funding acquisition. **Sarah E. Gilbert:** Writing – review & editing, Writing – original draft, Methodology, Investigation. **Hassan Gezzaz:** Writing – review & editing, Investigation, Formal analysis.

## Declaration of competing interest

The authors declare that they have no known competing financial interests or personal relationships that could have appeared to influence the work reported in this paper.

## Data availability

Data will be made available on request.

## Acknowledgements

This is a contribution to the Australian Research Council Linkage Project LP200100156 (Critical Metals from Complex Copper Ores) co-supported by BHP Olympic Dam. We appreciate constructive comments of two anonymous reviewers that assisted us in refining presentation of our work.

## References

Armstrong, J.T., 1988. Quantitative analysis of silicate and oxide minerals: Comparison of Monte Carlo, ZAF, and φ(ρz) procedures. In: Newbury, D.E. (Ed.), Microbeam Analysis. San Francisco Press, San Francisco, CA, USA, pp. 239–246.

Beauchemin, S., Chen, T.T., Dutrizac, D., 2008. Behaviour of antimony and bismuth in copper electrorefining circuits. Can. Metall. Q. 47, 9–26.

Belousov, I., Danyushevsky, L., Goemann, K., Gilbert, S., Olin, P., Thompson, J., Lounejeva, E., Garbe-Schönberg, D., 2023. STDGL3, a reference material for analysis of sulfide minerals by laser ablation ICP-MS: an assessment of matrix effects and the impact of laser wavelengths and pulse widths. Geostand. Geoanal. Res. 47, 493–508.

BHP Billiton, 2009 Olympic Dam Expansion. Draft Environmental Impact Statement 2009. Chapter 2. Existing Operations. www.bhp.com.

Campbell, C.M., Moats, M.S., 2019. Characterization and electrorefining of a copper anode with high lead, arsenic and bismuth. In: Proceedings, 58th Annual Conference of Metallurgists (COM) Hosting the 10th International Copper Conference.

Chakrabarti, D.J., Laughlin, D.E., 1984. The Bi—Cu (bismuth-copper) system. Bull. Alloy Phase Diagr. 5, 148–155.

Chen, T.T., Dutrizac, J.E., 1988. Mineralogical characterization of anode slimes – 1. anode copper from Inco's Copper Cliff copper refinery. Can. Metall. Quarterly 27, 91–96.

Chen, T.T., Dutrizac, J.E., 1989. A mineralogical study of the deportment and reaction of silver during copper electrorefining. Metall. Mater. Trans. B 20, 345–361.

Chen, T.T., Dutrizac, J.E., 1990a. Mineralogical characterization of anode slimes: Part V – nickel-rich copper anodes from the CCR division of Noranda Minerals Inc. Canadian Metall. Quarterly 29, 27–37.

Chen, T.T., Dutrizac, J.E., 1990b. The mineralogy of copper electrorefining. JOM 42, 39–44.

Chen, T.T., Dutrizac, J.E., 1991. Mineralogical characterization of anode slimes: Part 7. copper anodes and anode slimes from the Chuquicamata division of CODELCO-Chile. Can. Metall. Quarterly 30, 95–106.

Chen, T.T., Dutrizac, J.E., 1993. The mineralogical characterization of tellurium in copper anodes. Metall. Mater. Trans. B 24, 997–1007.

Chen, T.T., Dutrizac, J.E., 2005. Mineralogical characterization of a copper anode and the anode slimes from the La Caridad copper refinery of Mexicana de Cobre. Metall. Mater. Trans. B 36, 229–240.

Cook, N.J., Ciobanu, C.L., Ehrig, K., Slattery, A.D., Gilbert, S.E., 2022. Micron- to atomic-scale investigation of rare earth elements in iron oxides. Front. Earth Sci. 10, 967189.

Cook, N.J., Ehrig, K., Ciobanu, C.L., King, S.A., Slattery, A.D., 2024. Detailed characterisation of precious metals and critical elements in anode slimes from the Olympic Dam copper refinery, South Australia. Minerals Eng. 206, 108539.

Ehrig, K., Ciobanu, C.L., Verdugo-Ihl, M.R., Dmitrijeva, M., Cook, N.J., Slattery, A., 2023. Lifting the cloak of invisibility: gold in pyrite from the Olympic Dam Cu-U-Au-Ag deposit, South Australia. Am. Mineral. 108, 259–276.

Ehrig, K., McPhie, J., Kamenetsky, V.S., 2012. Geology and mineralogical zonation of the Olympic Dam iron oxide Cu-U-Au-Ag deposit, South Australia. In: Geology and Genesis of Major Copper Deposits and Districts of the World, a Tribute to Richard Sillitoe. Society of Economic Geologists, Littleton, CO, USA, pp. 237–268.

Ge, Y., Liu, Z., Yu, Z., Wang, H., Lu, X., Zhang, L., Xia, L., 2023. Distribution behaviors of As, Sb, Bi, Sn, Se, Te, Au and Ag between Cu and liquid metal phases in the Cu-Pb binary system at 500–1080°C. JOM 75, 1515–1529.

Gezzaz, H., Ciobanu, C.L., Slattery, A., Cook, N.J., Ehrig, K., 2023a. Cation inversion in slag magnetite: energy loss measurements of Fe-$L_3$ edge shift between atom columns. Mater Charact 204, 113224.

Gezzaz, H., Ciobanu, C.L., Cook, N.J., Ehrig, K., Slattery, A., Wade, B., Yao, J., 2023b. Copper-bearing magnetite and delafossite in copper smelter slags. Minerals 13, 1374.

Hait, J., Jana, R.K., Sanyal, S.K., 2009. Processing of copper electrorefining anode slime: a review. Mineral Proc. Extract, Metall. (trans. IMM C) 118, 240–252.

Kanari, N., Allain, E., Shallari, S., Diot, F., Diliberto, S., Patisson, F., Yvon, J., 2019. Thermochemical route for extraction and recycling of critical, strategic and high value elements from by-products and end-of-life materials, part I: treatment of a copper by-product in air atmosphere. Mater. 12, 1625.

Moats, M.S., Wang, S., Kim, D., 2012. A review of the behaviour and deportment of lead, bismuth, antimony and arsenic in copper electrorefining. In: Wang, S. (Ed.), T.T. Chen Honorary Symposium on Hydrometallurgy, Electrometallurgy and Materials Characterization. John Wiley & Sons, Inc, Pittsburgh, PA, USA, pp. 3–21.

Moats, M.S., Filzwieser, A., Wang, S., Davenport, W.G., Robinson, T., Siegmund, A., 2019. Global survey of copper electrorefining: 2019 world tankhouse operating data. In: Proceedings, 58th Annual Conference of Metallurgists (COM) Hosting the 10th International Copper Conference.

Mubarak, Z., Antrekowitsch, H., Mori, G., 2007. Passivation behaviour of copper anodes with various chemical composition. In: Proceedings, 136th TMS Annual Meeting, pp. 225–234.

Schlesinger, M.E., Sole, K.C., Davenport, W.G., Alvear Flores, G.R.G., 2022. Extractive metallurgy of copper, 6th edition. Elsevier, Amsterdam, p. 593.

Subramanian, P.R., Perepezko, J.H., 1993. The Ag-Cu (silver-copper) system. Bull. Alloy Phase Diagr. 14, 62–75.

Wenzl, C., Filzwieser, A., Antrekowitsch, H., 2007a. Review of anode casting – part I: chemical anode quality. Erzmetall 60, 77–83.

Wenzl, C., Filzwieser, A., Antrekowitsch, H., 2007b. Review of anode casting – part II: physical anode quality. Erzmetall 60, 83–88.

Wenzl, C., Filzwieser, I., Mori, G., Pesl, J., 2008. Investigations on anode quality in copper electrorefining. BHM Berg- Huettenmaenn. Monatsh. 153, 91–96.